# Sensorless Induction Motor Drive with a Single DC-Link Current Sensor and Instantaneous Active and Reactive Power Feedback

Slobodan N. Vukosavic, *Member, IEEE,* and Aleksandar M. Stankovic, *Member, IEEE*

***Abstract*—This paper proposes a novel torque and speed control structure for low-cost induction motor variable-speed drives with a single dc-link current sensor. The controller is based on reconstruction of the active and instantaneous reactive power from the dc-link current without the use of a shaft sensor. An effective way of achieving tracking of set values of motor torque and flux is to base the estimation on the instantaneous active $(P)$ and reactive power $(Q)$. The paper proposes a way for extracting instantaneous $P$ and $Q$ information from the dc-link current and the pulsewidth modulation pattern. Torque and flux controllers suitable for general purpose and traction applications are proposed. The paper presents analytical considerations, straightforward design guidelines, and experimental results obtained from a traction system with a battery-fed three-phase inverter and a 7.5-kW traction motor.**

***Index Terms*—AC drives, induction motor, instantaneous active and reactive power, sensorless operation.**

## I. Introduction

THE three-phase hard-switched voltage-sourced inverter (VSI) with a three-phase front-end rectifier and dc-link circuit is the most common frequency converter topology. It is widely used in industrial and appliance fields. The VSI with six diodes and six insulated gate bipolar transistors (IGBTs) is the workhorse of uninterruptible power supply (UPS) systems, power-factor compensators [1], and static var compensators [2]. The availability of a set of three-phase voltages with continuously variable amplitude and frequency provided the impetus for wide application of ac motor variable-speed drives [3]–[11]. These can be divided into high-performance drives (mostly sensored servo drives) and general-purpose drives characterized by medium performance requirements and low cost (operating mostly with standard sensorless motors).

High-performance drives are characterized by an ever-increasing demand for faster and more precise response of velocity and position control loops. These requests originate from the need for improved quality and productivity of machining centers and robots. Consequently, the price, component, and sensor count in a high-performance servo system are not the most important figures of merit.

The majority of variable-speed drives are used in general-purpose applications such as pumps, fans, compressors, and traction, where the drive has to be capable of speed variation with a moderate performance. In such applications, the most relevant factors are ease of cabling and setup, robustness, and low overall cost. Reduction of the total number of sensors offers savings in sensor cost, simplifies cabling and maintenance, and in most cases has a potential to increase the reliability of the system. At the same time, digital signal processor (DSP) controllers and software-based algorithms do not contribute to the overall price nearly as much. Therefore, substantial research effort is focused on improving the performance of induction motor drives operating without the shaft feedback.

The three-phase VSI topology allows for further reduction of the number of current sensors through the reconstruction of the phase currents from the dc-link current signal. Green [3], [4] was among the first to propose such a scheme; using a sample-and-hold or filter-and-hold technique, phase currents are "seen" through the dc-link current signal in time spans when the corresponding switching takes place. The space-vector modulation [5] with optimal voltage-vector sequencing allows for two (out of three) phase currents to be detected in each switching period, and the third is recovered from these two. Certain operating conditions such as low modulation index, the reference vector close to $(n\pi/3)$, or overmodulation make the phase currents unobtainable directly from the dc-link current. Conditions for reconstruction of instantaneous values of phase currents further deteriorate in cases of long power cables and imperfections of current sensors. To overcome these problems, Habetler [6] proposes a discrete modulation technique using exclusively nonzero voltage vectors. While effective in improving reconstruction of phase currents, this approach increases the current ripple and associated losses. Xue [7] proposes elimination of narrow pulses from a pulsewidth modulation (PWM) period, and their shifting into the succeeding cycle where adjusted longer pulses will compensate for the volt-seconds lost in the previous cycle. This approach is more suitable for phase current reconstruction, since current sampling is easier when the dc-link current comprises wider pulses; on the other hand, this approach delays the current feedback signals and makes the current control more difficult.

The current sampling process is prone to aliasing, as phase currents have a strong spectral component at the PWM frequency (i.e., the current ripple). Moynihan [8] proposed that the dc-link current be sampled at the center of each pulse, so that effects of the ripple are suppressed. Under narrow-pulse conditions, he proposed a modification of the PWM algorithm based on a complementary alteration of voltage vectors. Riese [10] re-

Manuscript received April 19, 1998; revised August 10, 2000. Abstract published on the Internet September 6, 2000.

S. N. Vukosavic is with the Department of Electrical Engineering, University of Belgrade, Belgrade, Yugoslavia.

A. M. Stankovic is with the Department of Electrical and Computer Engineering, Northeastern University, Boston, MA 02115 USA.

Publisher Item Identifier S 0278-0046(01)10004-3.

solves the problems related to narrow pulses by introducing alternating pulsewidth errors in successive PWM periods; voltage pulses are adjusted in width to make the dc-link current fragments longer and, thus, easier to capture. Blaabjerg [11] proposed a method and a current sensor arrangement for the acquisition of true instantaneous phase current from the dc-link signal, together with the short-circuit and ground-fault protections implemented with only one current sensor. Peng and Fukao [15] report another approach relevant for the development presented here. Their scheme relies on complete current measurements, and uses the instantaneous reactive power of the magnetizing inductance in a feedback control algorithm that produces an estimate of the speed of the synchronous reference frame.

Control of the induction motor based on explicit current regulation requires high-bandwidth current measurements. Sensing circuitry must be capable of fast, ripple- and noise-free sampling of dc-link current fragments. Signals acquired in this manner remain sensitive to narrow-pulse problems, and may further deteriorate if the cable capacitance causes spurious oscillations in the dc-link waveform. These problems can be avoided if the average value of dc-link current or other low-pass-filtered quantity related to motor current, flux, or torque is observed. In this paper we propose a novel solution intended for medium-performance general applications such as traction. The basis for flux and voltage control is the acquisition of instantaneous active $(P)$ and reactive $(Q)$ power signal from the dc-link current waveform and the space-vector-modulation switching pattern. We use the notion of instantaneous $P$ and $Q$ to denote quantities averaged over a very short cycle of the PWM pattern. These quantities reduce to well-known active (real) and reactive power over a fundamental period of the supply waveforms at machine terminals, justifying the terminology. Averaging of dc-link current fragments and their correlation with the PWM pattern provide $P$ and $Q$ signals with little ripple that are free from problems related to the power cable length and deadtime compensation. The paper presents analytical considerations in parallel with experimental waveforms. The proposed structure for torque and flux control is based on instantaneous $P$ and $Q$ signals, and includes self-synchronization of the rotational $dq$ frame. Starting with $P$ and $Q$ signals, the controller derives flux and torque estimates, followed by the $dq$-frame velocity and reference voltage commands $Ud$ and $Uq$. The main aim is to regulate the motor torque in general-purpose applications; we do not address issues common to high-performance drives, such as speed and position tracking. The paper contains straightforward design guidelines and their experimental verification on a sensorless three-phase traction drive prototype with a 7.5-kW induction motor.

## II. Derivation of the Average Active and Reactive Power From the Dc-Link Current Waveform and the PWM Pattern

The hard-switched three-phase VSI is the most widely used converter topology in general-purpose ac drives [16]. Due to the discrete nature of the output phase voltages, only seven distinct voltage vectors, listed in Table I, can be generated.

In a stationary $(\alpha - \beta)$ plane, the nonzero vectors form a hexagon, and the standard practice is to approximate any reference vector over a switching cycle with a set of three vectors [19] (two of them nonzero and adjacent to the reference). We assume that the phase "$a$" and the $\alpha$ axis are aligned with V1. While the sequencing of the vectors does not influence the average voltages, it affects switching losses, common-mode quantities, and current ripple, and can be adjusted to meet various goals in practice. Each voltage vector within the sequence corresponds to a state of the VSI power switches. These states determine the way in which phase currents are mirrored by the dc-link current. Due to restrictions posed by the VSI topology, the dc-link current may be zero (for states 000 and 111), $+Ia$, $-Ia$, $+Ib$, $-Ib$, $+Ic$, $-Ic$, (for active states), as shown in Table I, where $Ia$ denotes the current in phase "$a$," etc.

TABLE I
DC-Link Current for Eight VSI Switching States (ABC)

| DC-LINK CURRENT FOR 8 VSI SWITCHING STATES (ABC): | | | | | |
|---|---|---|---|---|---|
| V0 = 000 | ⇒ | IDC = 0 | V4 = 100 | ⇒ | IDC = - IA |
| V1 = 100 | ⇒ | IDC = + IA | V5 = 100 | ⇒ | IDC = + IC |
| V2 = 110 | ⇒ | IDC = - IC | V6 = 100 | ⇒ | IDC = - IB |
| V3 = 010 | ⇒ | Idc = + Ib | V7 = 100 | ⇒ | IDC = 0 |

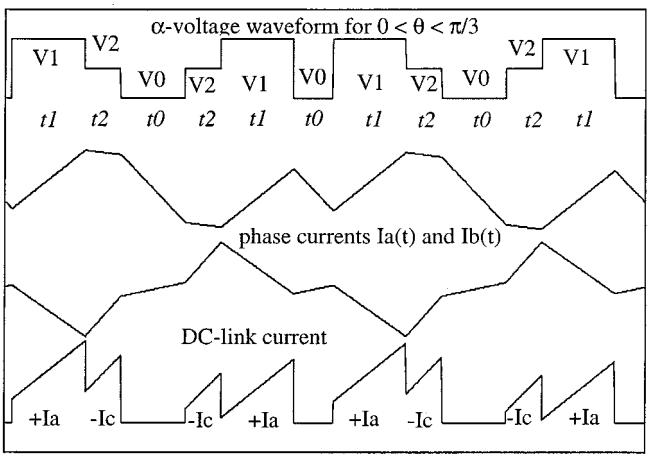


Fig. 1. DC-link current waveform versus the PWM pattern for $0 < \theta_u < \pi/3$.

Assuming the angle of the voltage reference $0 < \theta_u < \pi/3$, the most common PWM algorithm involves the sequencing of vectors V1, V2, and V0, as shown in Fig. 1. The time segments $t1$, $t2$, and $t3$ are found from the reference vector amplitude and angle [16], [19]. From Table I, the dc-link current equals $+Ia$ during the time interval $t1$, $-Ic$ during the time interval $t2$, and zero during the time $t0$. The waveforms shown in Fig. 1 are obtained for the reference vector in the first sector of the hexagon $(0 < \theta_u < \pi/3)$, and analogous waveforms are easily generated for other sectors. We will show below that the instantaneous active $(P)$ and reactive $(Q)$ power can be derived from the dc-link current averaged over a PWM cycle. The fragment $+Ia$ corresponds to V1, i.e., the active vector located in the clockwise (CW) direction from the reference. Similarly, the fragment $-Ic$ corresponds to the application of V2, which is a vector in counterclockwise (CCW) direction from the reference. It will turn out that $P$ and $Q$ can be determined as the sum of CW and CCW fragments, respectively. Assuming that the instantaneous (and, consequently, the average) reactive power consumed by the in-

duction motor is positive, there is a (positive) angle $\varphi$ by which the voltage reference leads the magnetomotive force. Let the magnitude of the current vector be $(i_\alpha^2 + i_\beta^2) = I^2$; if switching ripple is neglected, the phase currents are

$$\begin{aligned} i_a(t) &= I\cos(\theta_u - \varphi) \\ i_b(t) &= I\cos(\theta_u - 2\pi/3 - \varphi) \\ i_c(t) &= I\cos(\theta_u - 4\pi/3 - \varphi). \end{aligned} \tag{1}$$

In a steady state, $\theta_u = \omega_t$, and the phase currents are sinusoidal and symmetric. During transients involving several periods of the supply voltage, amplitude $I$, phase $\varphi$, and reference $\theta_u$ may vary. For such operation, we can derive active and reactive power (averaged over a period $2\pi/\omega$ of the supply waveforms) from the voltage vector and from current components aligned $(I_P = I\cos(\varphi))$ and orthogonal $(I_Q = I\sin(\varphi))$ to it

$$P = KUI_P \tag{2}$$

$$Q = KUI_Q \tag{3}$$

where $K = 3/2$ for Clark's two phase to three phase transformation commonly used in the motor modeling, while $U$ stands for the voltage amplitude $(u_\alpha^2 + u_\beta^2 = U^2)$ and equals the peak of the motor phase voltage.

In experimental setup, it is easy to distinguish the duration of CW segments (V1 in the first sector, dc-link current $+ia$) from the CCW segments (V2 in the first sector, DC-link current $-ic$). Analog switches with filter-and-hold circuitry are used in our setup to separate dc-link fragments $I_{\rm CW}$ and $I_{\rm CCW}$; a key observation is that CW vectors in sectors 1, 3, and 5 $(2n < 3\theta_u/\pi < 2n+1)$ have two zeros in their switching code, while CW vectors in sectors 2, 4, and 6 $(2n+1 < 3\theta_u/\pi < 2n)$ have only one zero.

Average values of $I_{\rm CW}$ and $I_{CCW}$ can be calculated in each sector of the hexagon. Let $T$ denote the PWM switching period, $E_{\rm DC}$ the dc-bus voltage, and $m$ the modulation index; then, assuming a constant speed of the reference vector in the first sector

$$\begin{aligned} I_{\rm CW}^{AV} &= \frac{1}{\pi/3}\int_0^{\pi/3} i_a(\theta)\frac{t_1(\theta)}{T}\,d\theta \\ &= mI\left[\frac{1}{2}\cos(\varphi) - \frac{1}{2\sqrt{3}}\sin(\varphi) + \frac{3}{2\pi}\sin(\varphi)\right] \\ I_{CCW}^{AV} &= \frac{-1}{\pi/3}\int_0^{\pi/3} i_c(\theta)\frac{t_2(\theta)}{T}\,d\theta \\ &= mI\left[\frac{1}{2}\cos(\varphi) + \frac{1}{2\sqrt{3}}\sin(\varphi) - \frac{3}{2\pi}\sin(\varphi)\right]. \end{aligned} \tag{4}$$

From these two quantities, we can easily derive active and reactive power averaged over a period of the supply waveforms; in particular,

$$\begin{aligned} I_{\rm CW}^{AV} + I_{\rm CCW}^{AV} &= mI_{\frac{\sqrt{3}}{2}}\cos(\varphi) = \frac{P^{AV}}{E_{\rm DC}} = \frac{P^{AV}}{\sqrt{3}U_{\max}} = K_U P^{AV} \\ I_{\rm CW}^{AV} - I_{\rm CCW}^{AV} &= mI\frac{\sqrt{3}}{3}\left[\frac{3}{\pi} - \frac{1}{\sqrt{3}}\right]\sin(\varphi) = K_X\frac{Q^{AV}}{E_{\rm DC}} \\ &= K_X\frac{Q^{AV}}{\sqrt{3}U_{\max}} = K_X K_U Q^{AV} \end{aligned} \tag{5}$$

where $U_{\max}$ stands for the maximum available $\alpha - \beta$ voltage, $Kx \approx 0.377$ is constant, while $K_U$ depends on the dc-bus voltage $E_{\rm DC}$ (which is most often constant as well). The signals obtained in this way may be used to monitor the behavior of an ac drive close to a steady state (i.e, over time intervals longer than $2\pi/\omega$). However, they cannot be used as feedback signals in the closed-loop control of flux and torque unless the required closed-loop response is much longer than the time constants of the motor's electrical subsystem, which is rarely the case. Response times of several tens of milliseconds are often required in medium-performance drives. We are thus motivated to look for signals that will reduce to $P$ and $Q$ in (3) when averaged over the supply period, but will have a sufficiently high bandwidth to make possible a satisfactory response of the torque and flux control loops while being derived from the dc-link current measurement. Assuming the PWM frequency to be above 1 kHz, the feedback signals averaged over one PWM period $T$ are as good for control purposes as instantaneous signals. For example, one PWM period averaging is advantageously used even in stator current controllers that have much shorter response time than the controllers of medium-performance ac drives that we consider [20].

## III. Derivation of Instantaneous Active and Reactive Power

Referring to Fig. 1, we can find the "medium-term" averages of $I_{\rm CW}$ and $I_{\rm CCW}$ over one PWM period $T$ as

$$\begin{aligned} I_{\rm CW}^{MED} &= \frac{1}{T}\int_{nT}^{(n+1)T} I_{\rm CW}(t)\,dt = \frac{1}{T}\int_{nT}^{nT+t1} i_a(t)\,dt \\ &= mI\cos(\vartheta - \varphi)\sin(\pi/3 - \vartheta) \\ I_{\rm CCW}^{MED} &= \frac{1}{T}\int_{nT}^{(n+1)T} I_{\rm CCW}(t)\,dt = \frac{1}{T}\int_{nT+t1}^{nT+t1+t2} -i_c(t)\,dt \\ &= mI\cos(\vartheta - \varphi - \pi/3)\sin(\vartheta). \end{aligned} \tag{6}$$

In this equation, $\theta$ is the spatial displacement between the voltage reference vector and the active voltage vector in the CW direction; for example, in sector 1, the CW vector is V1 and $\theta = \theta_u - \arg(V1) = \theta_u$. Given $\theta$, the medium-term averages of $I_{\rm CW}$ and $I_{\rm CCW}$ can be determined in all six sectors from (6). The sum and difference of the two currents is

$$\begin{aligned} C &= T\left(I_{\rm CW}^{MED} + I_{\rm CCW}^{MED}\right) = mTI\frac{\sqrt{3}}{2}\cos(\varphi) \\ D &= T\left(I_{\rm CW}^{MED} - I_{\rm CCW}^{MED}\right) = mTI\left(-\tfrac{1}{2} + \cos(\delta)\right)\sin(\varphi) \\ &\quad + mTI\sin(\delta)\cos(\varphi) \end{aligned} \tag{7}$$

where $\delta$ equals $\pi/3 - 2\theta$. Signals $C$ and $D$ in (7) can be used to determine instantaneous values of $P$ and $Q$; a practical arrangement that yields ripple-free $P$ and $Q$ is shown in Fig. 2.

Filtered and sampled $C$ and $D$ are inputs of the A/D converter, whose output is fed into the digital drive controller. The signal processing outlined in Fig. 2 is implemented in software, and requires $\delta = \pi/3 - 2\theta$ as an input. The PWM pattern is generated by the drive controller; starting with the magnitude $(U)$ and the angle $(\theta_u)$ of reference (1), IGBT gating pulses are derived [16], [19] together with the control signals that determine states of analog switches CW and CCW in Fig. 2. Additional details about the experimental setup are provided in the Appendix.

Due to unavoidable lockout time (i.e., deadtime) insertion, the voltages at the motor terminals will differ from the ones de-

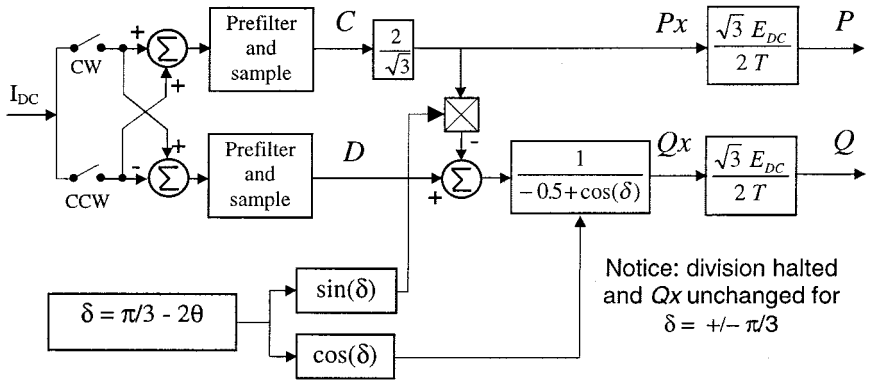


Fig. 2. Derivation of instantaneous $P$ and $Q$ signals from the dc-link current.

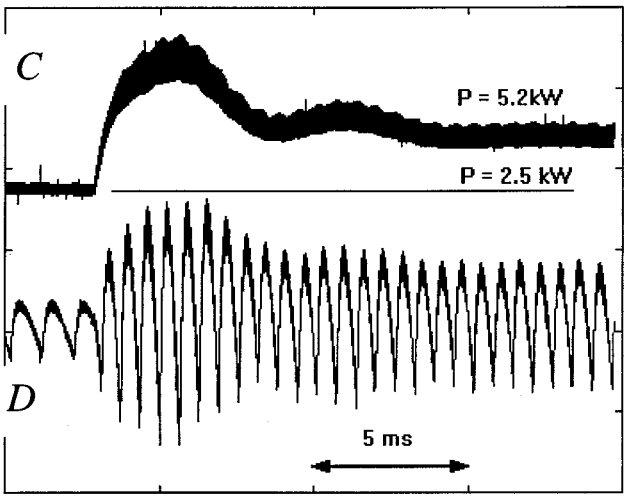


Fig. 3. Traces of $C$ and $D$ signals obtained from the experimental setup running in open loop. Supply frequency is changed in a stepwise manner from 16 to 25 Hz, having a constant ratio $U/f$ = and the motor connected to frictional load, delivering rated torque at 16 Hz. $C$ (upper trace) and $D$ (lower trace), first-order $\tau = 1$ ms low-pass filtering is imposed on both signals.

termined by the PWM pattern. The instantaneous active power $P$ is weakly affected by the lockout time, as it corresponds (5) and (7) to the average value of the dc-link current over the PWM cycle. Calculations of the instantaneous reactive power $Q$, on the other hand, require precise timing of commutation of CW–CCW switches (V1 to V2 transition in Fig. 1, making them sensitive to lockout time. Note in Fig. 1 that the transition from V1 to V2 depends on the sign of the phase current $ib$: in the case $ib > 0$, the transition lags with respect to the gating signals by the lockout time $\Delta t_{\rm lock}$; if $ib < 0$, the lockout time has no effect, and the actual switching coincides with the PWM pattern. It turns out that if the stator current lags behind the voltage by at least $\varphi = \pi/6$, then the lockout time will not affect the calculation of the reactive power $Q$. In cases where the current is less delayed with respect to the voltage (i.e., when $\varphi = \text{arctg}(Q/P) < \pi/6$), there is a need for lockout-time compensation. As the phase lag change $\Delta\varphi$ within a PWM cycle is relatively small, the detection of CW–CCW switching instant is based on $P$ and $Q$ estimates in the preceding PWM cycle. The compensation is implemented in software: the CW to CCW transition (Fig. 2) is delayed by $\Delta t_{\rm lock}$ with respect to $nT + t1$ (see also Fig. 1); the opening of the CCW switch is delayed by $\Delta t_{\rm lock}$ regardless of the lockout time, as it has no detrimental consequences (active vectors are followed by a zero vector V0 or V7, and the dc-link current is zero in either case).

Fig. 3 presents experimental traces of $C$ and $D$ signals. These are passed through a low-pass filter integrated in the "Prefilter and sample" blocks in Fig. 2. The filter cutoff frequency is close to 150 Hz, but residual PWM-generated noise is still visible in both traces. While the upper $C$ trace (related to the active power) shows no low-frequency variations, the $D$ trace contains a ripple at six times the fundamental frequency, as expected from the definition of $\delta$ in Fig. 2 and from (7). It is, thus, necessary to further process the two signals, as shown in the right portion of Fig. 2. The $C$ and $D$ signals are integrated over each PWM cycle of length $T$, and fed to A/D converters at the end of cycle; simultaneously, integrators are reset via a dedicated pair of analog switches placed in parallel with the integrators capacitors. The remaining blocks in Fig. 2, including calculation of $\theta$ and $\delta$, are implemented in software.

Experimental traces of $Px$ and $Qx$ are shown in Fig. 4; these signals are proportional to instantaneous values of $I_P$ and $I_Q$ components of stator currents (3) and are ripple free (which will be used for control purposes later). Note in Fig. 2 that the reactive power calculation has to be suspended when the voltage angle $\theta_u$ equals exactly a multiple of $\pi/3$. This produces no effect on $P$ and $Q$ when the supply frequency $d\theta_u/dt$ has any nonzero value.

## IV. Acquisition of the Stator Current Projections From Instantaneous Active and Reactive Power in Arbitrary Frame of Reference

The amplitude $U$ and spatial orientation $\theta_u$ of the stator voltage determine the voltage components in synchronous $(d$–$q)$ and stationary $(\alpha$- -$\beta)$ reference frames [16]. The stator current vector is delayed by angle $\varphi$ with respect to the voltage. During transients that involve several periods of the fundamental, the angle $\varphi$ varies and determines changes of the active $(I_P = I\cos\varphi)$ and the orthogonal $(I_P = I\sin\varphi)$ current component. The $x$–$y$ reference frame is selected so that $U_Y = U, U_X = 0$, yielding $I_Y = I_P$ and $I_X = I_Q$. Then, the active and reactive power (averaged over a period $T$ of

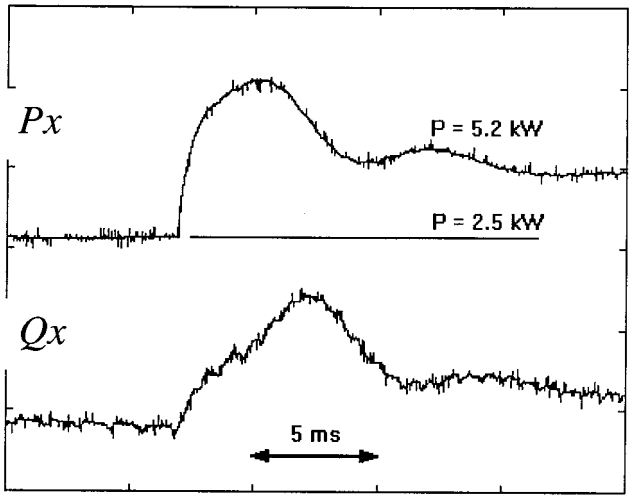


Fig. 4. Experimental traces of $Px$ (upper) and $Qx$ (lower) signals obtained from the experimental setup in the open loop; all test conditions are unchanged from Fig. 3.

the switching frequency) can be calculated from current and voltage components

$$P = KUI_P = K(U_\alpha I_\alpha + U_\beta I_\beta) = K(U_d I_d + U_q I_q)$$
$$Q = KUI_Q = K(U_\beta I_\alpha - U_\alpha I_\beta) = K(U_q I_d - U_d I_q). \quad (8)$$

The components of the voltage vector in arbitrary reference can be determined, provided that the lockout-time imperfections are negligible, or compensated for. Hence, from $P$ and $Q$ signals (Fig. 4), we can derive the current vector components as follows:

$$i_\alpha = \frac{1}{K}\frac{Pu_\alpha + Qu_\beta}{u_\alpha^2 + u_\beta^2} = \frac{1}{K}\frac{Pu_\alpha + Qu_\beta}{U^2}$$
$$i_\beta = \frac{1}{K}\frac{Pu_\beta - Qu_\alpha}{u_\alpha^2 + u_\beta^2} = \frac{1}{K}\frac{Pu_\beta - Qu_\alpha}{U^2}$$
$$i_d = \frac{1}{K}\frac{Pu_d + Qu_q}{u_d^2 + u_q^2} = \frac{1}{K}\frac{Pu_d + Qu_q}{U^2}$$
$$i_q = \frac{1}{K}\frac{Pu_q - Qu_d}{u_d^2 + u_q^2} = \frac{1}{K}\frac{Pu_q - Qu_d}{U^2}. \quad (9)$$

The stator current components $i_\alpha$ and $i_\beta$ will be used later in the flux and torque controller of the sensorless induction motor drive.

## V. PQ-Feedback-Based Self-Synchronization of the DQ-Frame

In a majority of sensorless induction motor drives, decoupled torque and flux regulation is achieved by means of controllers implemented in the synchronous $d$–$q$ reference frame. The torque-related dynamics and control actions are along the $q$ axis, while the excitation loop is in the $d$ axis where voltage $U_d$ controls the flux. In essence, most sensorless control schemes resemble the direct field-oriented control, while the ways of obtaining the $d$–$q$ frame speed and orientation are specific for each scheme.

The speed $\omega_{dq}$ and position $\theta_{dq}$ of the synchronous reference frame may be derived from $\alpha$ and $\beta$ components of the stator, rotor, or air-gap flux. These components require observer structures which rely on the motor terminal quantities ($U_s$, $I_s$), and perform calculation and integration of the electromotive force vector. Some authors recommend phase-locked-loop (PLL)-like $dq$-frame synchronization mechanisms, where the frame speed $\omega_{dq}$ is adjusted to achieve the flux vector that is orthogonal on the $q$ axis. Others [12] select the frame speed according to the current error $\Delta i_q$, resulting in a closed-loop structure similar to PLL. While an estimate of the stator currents $i_\alpha$ and $i_\beta$ can be derived from $(P, Q)$, it is not equivalent to direct measurements in terms of the capability to provide a stable $d$–$q$ frame synchronization. Besides the residual noise in $(P, Q)$ signals (Figs. 3 and 4), the detection circuit has a disadvantage common to all dc-link-based phase current reconstruction schemes—the phase current information becomes unreliable if the voltage remains for a long time close to a multiple of $\pi/3$. For this reason, our $d$–$q$ frame synchronization derives the $d$–$q$ frame location directly from the voltage amplitude $U$ and instantaneous active and reactive power

$$u_{ds} = R_s i_{ds} + \frac{d\psi_{ds}}{dt} - \omega_{dq}\psi_{qs} \quad (10)$$
$$u_{qs} = R_s i_{qs} + \frac{d\psi_{qs}}{dt} + \omega_{dq}\psi_{ds} \quad (11)$$
$$U^2 = u_{ds}^2 + u_{qs}^2 = R_s^2(i_{ds}^2 + i_{qs}^2) + \omega_{dq}^2(\psi_{ds}^2 + \psi_{qs}^2) + 2R_s\omega_{dq}(\psi_{ds} i_{qs} - \psi_{qs} i_{ds}). \quad (12)$$

In (11) and (12), the voltage balance in the $d$ and $q$ axes is expressed in terms of stator current and flux components in the synchronous reference frame ($\omega_{dq}$ is the rotational speed of the $dq$-frame); $R_s$ is the stator resistance. Assuming that the frame is attached to the stator flux and that the flux amplitude is kept constant (which is a control objective), the time-derivative terms in (11) and (12) vanish. Consequently, (12) relates the voltage amplitude $U$ to the stator current, flux, and speed $\omega_{dq}$. Magnitudes of stator current and flux can be expressed in terms of $d$ and $q$ components as

$$i_s^2 = i_{ds}^2 + i_{qs}^2 \quad (13)$$
$$\psi_s^2 = \psi_{ds}^2 + \psi_{qs}^2. \quad (14)$$

If we additionally assume that the stator core losses are negligible at low speed, the input power to the motor can be expressed as

$$i_s^2 = i_{ds}^2 + i_{qs}^2$$
$$\psi_s^2 = \psi_{ds}^2 + \psi_{qs}^2$$
$$P_{\text{in}} = R_s i_s^2 + \omega_{dq}(\psi_{ds} i_{qs} - \psi_{qs} i_{ds}). \quad (15)$$

Replacing (13)–(15) into (12), we can express the voltage magnitude $U$ in terms of the flux magnitude, instantaneous $P$ and $Q$, the frame speed $\omega_{dq}$, and stator resistance $R_s$ as

$$U^2 = -R_s^2 i_s^2 + \omega_{dq}^2\psi_s^2 + 2R_s P_{\text{in}}$$
$$= \omega_{dq}^2\psi_s^2 + 2R_s P - \frac{R_s^2}{K^2U^2}(P^2 + Q^2). \quad (16)$$

Thus, provided that $U$, $\Psi_s$, $P$, $Q$ and the parameter $R_s$ are known, the $d$–$q$ rotational speed $\omega_{dq}$ can be derived from

$$|\omega_{dq}| = \sqrt{\frac{U^2 + \frac{R_s^2}{K^2U^2}(P^2 + Q^2) - 2R_s P}{\psi_s^2}}. \quad (17)$$

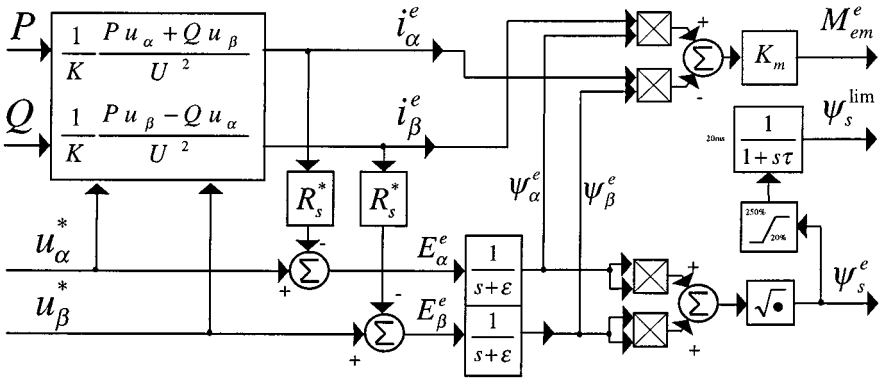


Fig. 5. Estimator of the electromagnetic torque, the stator flux, and the stator electromotive force based on the instantaneous reactive and active power signals obtained from the dc-link current by means of the structure shown in Fig. 2.

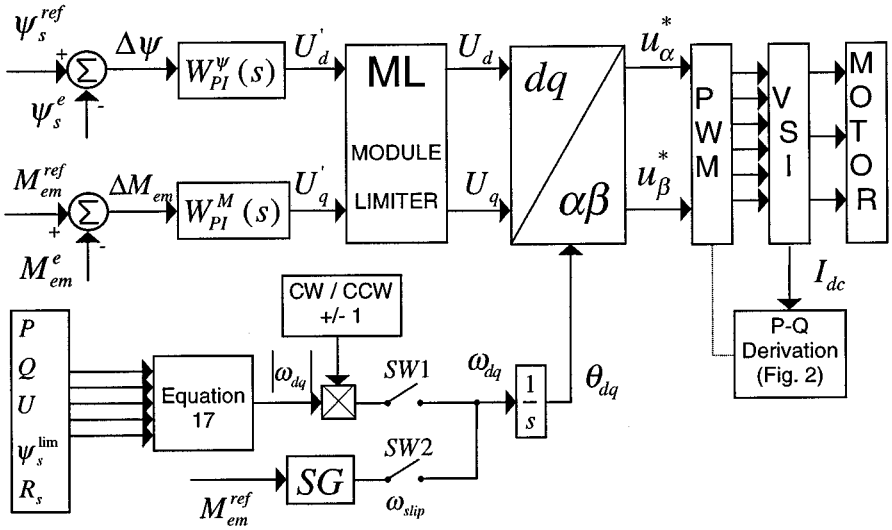


Fig. 6. Induction motor torque and flux controller based on the instantaneous active and reactive power feedback derived from the dc-link current.

The desired supply frequency $\omega_{dq}$ can be calculated from (17) in terms of the instantaneous active and reactive power. In experimental verifications shown later, the stator flux $\Psi_s$ is obtained from the flux estimator shown in Fig. 5. The estimated stator flux $\Psi_s$ is limited and filtered before being substituted in (17). Note that the $dq$-frame acquisition suggested in (17) requires no current, electromotive force, or flux-angle information. All that is needed are amplitudes of the voltage and the flux and the instantaneous $P$ and $Q$ signals; however, (17) provides only the magnitude of $\omega_{dq}$ and not the sign. Furthermore, due to the uncertainty in the value of stator resistance $R_s$, (17) may become unreliable when the supply frequency $\omega_{dq}$ drops below $R_s I_{\rm nom}/U_{\rm nom}$ (in p.u., where $U_{\rm nom}$ and $I_{\rm nom}$. are nominal voltage and current, respectively). For this reason, the drive controller shown in Fig. 6 produces the speed estimate depending on the operating mode.

It was observed in our experiments that the frame synchronization based on (17) (i.e., with SW1 on) performs well, even with the motor stopped, provided that the operating mode and the torque reference require no reversal of the frame of rotation. In traction applications, the drive with SW1 on accelerates from a standstill with controlled torque and flux, but it cannot brake down to zero speed unless SW2 is on, as the generation of the negative torque in the low-speed range requires a reversal of the $d$–$q$ frame and of the revolving field.

The "SG" block in Fig. 6 multiplies the torque reference with a constant gain $Rr/\Psi_s^2$ and provides the signal $\omega_{\rm slip}$ at the input of the selector switch SW2 ($R_r$. is the rotor resistance). If the rotor is at a standstill, then the calculated slip frequency equals the desired $dq$-frame speed. Thus, when SW1 is on and the rotor speed estimate $\omega_r = \omega_{dq} - \omega_{\rm slip}$ drops below the rated slip, the switches are rearranged (SW1 off, SW2 on), and the SG (slip gain) block defines the $dq$-frame speed and supply frequency, performing as an indirect field-oriented controller with a stalled rotor (Blaschke equation startup [21]). In a typical traction application, this operating mode occurs at the startup, or when the vehicle performs electrical braking down to the zero speed. When the drive accelerates, SW1 is switched back on, and the frequency estimate from (17) is used, with the sign of $\omega_r$ captured at the instant of commutation—indicated by the block "CW/CCW" in Fig. 6.

For applications with frequent reversals and requiring extremely low speed, it is essential to insure a smooth and stable transition between the open-loop (SW1=OFF) and the closed loop (SW1=ON) operation. In the experimental setup, we employed the frame synchronization selector shown in Fig. 7.

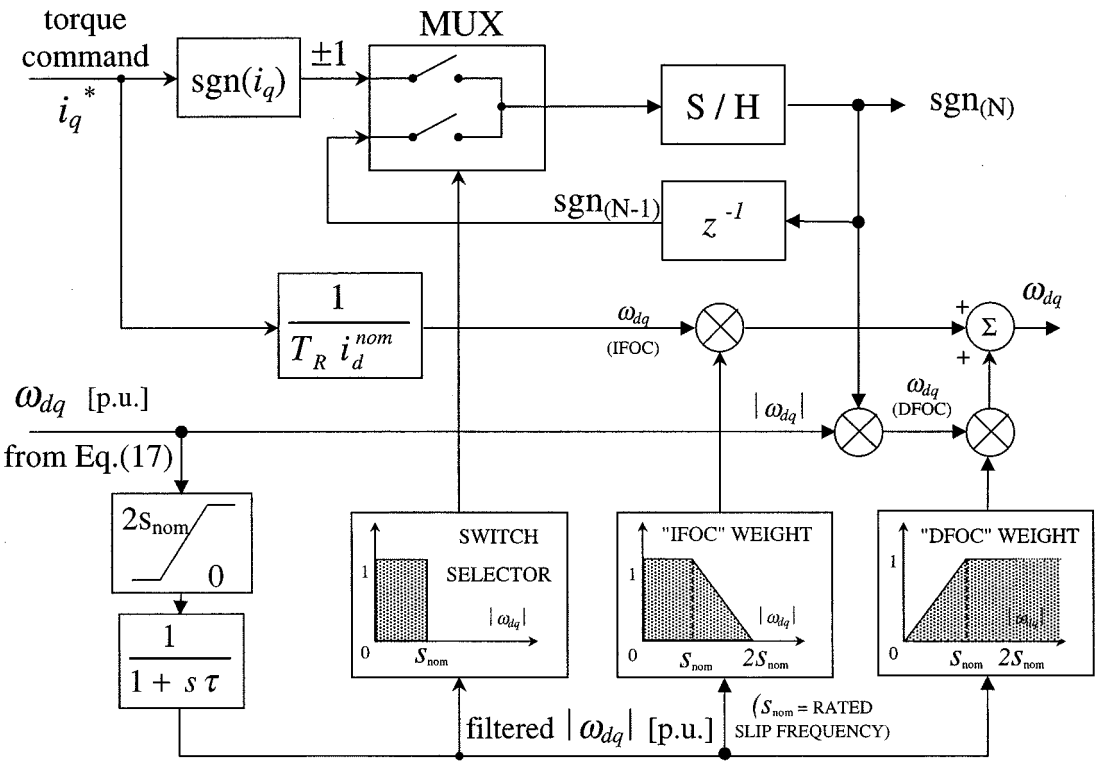


Fig. 7. Frame synchronization selector. At the startup and extremely low speeds, the IFOC-like calculator determines the $dq$-frame speed in an open-loop manner. The structure insures a smooth continuous transition to the closed-loop mode with the frame speed derived from (17) calculator.

The speed $\omega_{dq(\mathrm{IFOC})}$ is calculated from the $i_q$ current in an open-loop manner, assuming $\omega_r = 0$. The absolute value of the frame speed is found from (17) [$\omega_{dq(\mathrm{DFOC})}$ in Fig. 7] and used in the closed-loop mode. The sign of the closed-loop speed $\omega_{dq(\mathrm{DFOC})}$ (17) is determined from the sign of the open-loop speed $\omega_{dq(\mathrm{IFOC})}$, stored when the drive last operated in the $-s_{\mathrm{nom}} < \mathrm{EMF} < s_{\mathrm{nom}}$ mode.

Explicit switching is avoided and a smooth transition insured by taking a linear combination of $\omega_{dq(\mathrm{IFOC})}$ and $\omega_{dq(\mathrm{DFOC})}$ for the frame synchonization. The "IFOC" and "DFOC" weight coefficients (Fig. 7) change in a continuous way. Whenever the estimate (17) of the relative electromotive force (EMF) descends below the rated slip ($s_{\mathrm{nom}}$), the drive control converts fully in the open-loop mode ("IFOC"), while the closed-loop mode is solely active for the EMF above 2 $s_{\mathrm{nom}}$. Between the two thresholds, both modes affect the $dq$-frame speed in proportion to IFOC_WEIGHT and DFOC_WEIGHT coefficients. Experimental traces of the drive speed and torque at the startup and reversal demonstrate smooth transitions and prove the efficiency of the control structure proposed in Fig. 7.

## VI. Torque and Flux Controller Based on the Instantaneous Active and Reactive Power Feedback

Provided that the lockout time is properly compensated, the terminal voltage components will be determined by the digital signals loaded into the timers of the pulsewidth modulator. The structure shown in Fig. 2 returns the instantaneous $P$ and $Q$ signals obtained from the dc-link $I_{\mathrm{DC}}$ current and the PWM pattern. These two sets of data are used to obtain estimates of components of the stator current $i_{\alpha\beta}$ and the stator EMF $E_{\alpha\beta}$ in the stationary $\alpha - \beta$ frame, as seen in Fig. 5. Components of the stator flux are obtained through the integration [$1/(s+\varepsilon)$ block in Fig. 5] of $E_{\alpha\beta}$. Although all calculations are implemented in software, unavoidable offsets and integration at very low supply frequencies may result in difficulties, manifested in accumulation of errors and even saturation of discrete integrators. For these reasons, the integrators are chosen to be imperfect ("leaky"), and the corresponding parameter $\varepsilon$ is set to 0.04 rad/s. The estimated stator current and flux are used to calculate the flux magnitude, the electromagnetic torque, and the amplitude of the EMF, as shown in Fig. 5. These quantities are further used for calculation of the $dq$-frame speed and position, and for closing the flux and torque control loops (see Figs. 6 and 7).

The proposed controller is suitable for electric traction applications, where the reference command is often the reference torque. If the $dq$ frame is aligned with the rotor flux vector, the $d$ component of the current vector will control the flux, while the $q$ component will control the torque [16], [19]. If the $d$ axis is aligned with the stator current instead, the control behavior will be similar, except in transients when the leakage flux will cause a coupling between the flux and torque control loop.

The controller structure shown in Fig. 6 generates the voltage commands $U_d$ and $U_q$ depending on the difference between the reference and estimated values of the torque and flux. Unlike the stator flux field oriented controller, the proposed scheme does not use decoupling circuits. Instead, the flux $W^{\psi}(s)$ and torque $W^{M}(s)$ controllers perform the suppression of the coupling between the torque and flux control loops. Due to the particular

method used in acquisition of instantaneous $P$ and $Q$ signals, residual noise remains (Figs. 3 and 4), which limits the loop gains. For that reason, it is likely that the performance of the proposed controller cannot match that of direct field-oriented (DFOC) controllers with actual stator current measurements. However, the torque response times of a few milliseconds are achievable (as we show in the next section), satisfying the performance specifications for most general purpose and traction drives.

Test runs with an induction motor (see the Appendix for parameters) were performed with proportional plus integral (PI) flux $W^{\psi}(s)$ and torque $W^{M}(s)$ controllers. The proportional gain $kp_d$ in the $d$-axis is set to 1 p.u., i.e., a flux error equal to the rated flux produces a voltage step in $U_d$ equal to the nominal voltage; the $q$-axis gain $kp_q$ is set to 0.33 p.u. Integral gains are chosen to place the controller zeros at $z_d = ki_d/kp_d$ at 10 rad/s and $z_q = ki_q/kp_q$ at 24 rad/s, respectively. The gain $kp_q$ has a very significant influence on the performance; it is limited by the signal noise and by the short time constants in the $q$ axis governed by the equivalent leakage inductance $L_e$. Voltage commands $U'_d$ and $U'_q$ may exceed the voltage limits determined by the dc-bus voltage and VSI characteristics. Instead of limiting the components separately, the block "ML" in Fig. 6 restricts the magnitude of the voltage vector. The spatial orientation of the voltage vector remains unchanged, i.e., the angle corresponding to $(U_d, U_q)$ is the same as the angle of $(U'_d, U'_q)$. The voltage commands are converted to the stationary reference frame using the previously described synchronization procedure.

## VII. Experimental Results

The described control structure was verified experimentally in a series of test runs with a four-pole 7.5-kW induction motor coupled to a dc machine (with disconnected armature) serving as an inertial load. Motor data are in the Appendix, together with brief descriptions of the control circuitry, the drive digital controller and the three-phase inverter supplying the motor. The dc-link current is used as the only feedback signal. The DSP board is programmed to extract the instantaneous active and reactive power from the dc-link information and the PWM patter generated by the TMS320E14 device capture/compare subsystem.

In all experiments presented here, the $dq$-frame speed is calculated from (17) and Fig. 7; the lockout time is compensated in software, unless otherwise indicated. The voltage reference $u^*_{\alpha\beta}$ (Fig. 7) is adjusted by adding the constant amplitude vector $\Delta u_{\alpha\beta} = |\Delta u_{\alpha\beta}| = k\Delta t_{\rm lock} f_{\rm PWM} E_{\rm DC}$, with the spatial orientation $\arg(\Delta u_{\alpha\beta}) = \theta_u - \varphi$ where $\theta_u$ is the voltage reference angle and $\varphi = \arctan(Q/P)$. At very low supply frequencies ($\omega_{dq}/2\pi < 0.2$ Hz), $\Delta u_{\alpha\beta}$ is aligned with the voltage reference.

Variables internal to the control algorithm (such as the estimated flux and torque) are available during tests at D/A converter outputs of the drive controller board. The electromagnetic resolver on the dc brake was connected to a resolver to digital peripheral module of the control board, allowing monitoring of the shaft speed through a dedicated D/A port.

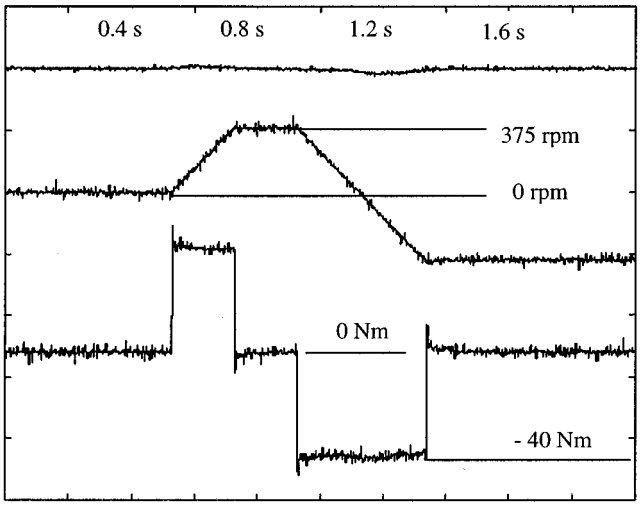


Fig. 8. Experimental traces of estimated flux (top trace), measured shaft speed (middle trace), and the estimated torque (bottom trace); during the drive acceleration and reversal, the stator resistance is set to correct value.

Experimental traces shown in Fig. 8 correspond to the case where the drive accelerates from standstill ($\omega_R = 0$), reaches the set speed, and makes the reversal with the correctly set stator resistance. The estimated torque waveform and the constant slope of the shaft speed confirm a good response of the drive and a smooth open–closed-loop mode transition. At the next step of algorithm evaluation, attempts were made to accelerate the drive from standstill *without* the lockout time compensation. The acceleration was very sluggish from standstill, and an acceptable torque transient is obtained only when starting speed is above 75 r/min (the case shown in Fig. 9. This finding confirms that lockout compensation is critical at very low speeds in control architectures in which terminal voltages are not explicitly measured. The second operating mode (SW2 on in Fig. 6) is less sensitive to the voltage error caused by the lockout time, and thus better suited for the start of the drive (Fig. 7.)

Sensorless induction machine control schemes are known to be sensitive to variations in parameters such as stator resistance. In the absence of a shaft sensor, flux, torque, and speed information is extracted from a subset of terminal voltages and currents. This is true regardless of the structure of the controller. The EMF becomes much smaller than the ohmic voltage drop $R_s I_s$ at very low speeds, and the variations in the stator resistance $R_s$ may limit the performance of the drive. We explored this issue by observing the drive response for $R_s$ settings that are approximately $\pm 20\%$ detuned from the true value. This is the range of variations that may be encountered due to extreme temperature variations. A substantial improvement (errors typically less than 10%) may be obtained by estimating the value of $R_s$ using a simple first-order thermal model, as suggested in [21] (which was not implemented in our setup).

In Fig. 10, we display the drive responses for the case when $R_s$ is overestimated (i.e., the value used in calculations is approximately 20% above the true value), while in Fig. 11 we show the drive responses when $R_s$ is underestimated by the same amount. The underestimated case (Fig. 11) results in acceptable overall performance, as the average torque is only slightly lower

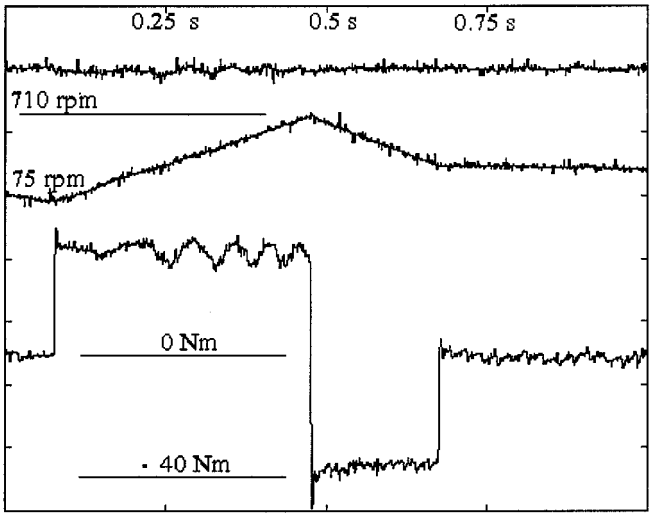


Fig. 9. Experimental traces of the estimated flux $\Psi_s^e$ (top trace), measured shaft speed $\omega_R$ (middle trace), and the estimated torque $M_{em}^e$ (bottom trace). No lockout time compensation is used, and the stator resistance used within the controller is set to correct value.

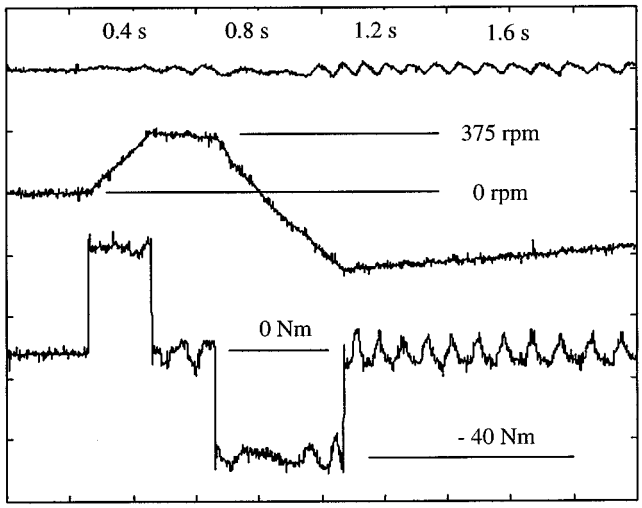


Fig. 10. Experimental traces of the estimated flux $\Psi_s^e$ (top trace), measured shaft speed $\omega_R$ (middle trace), and the estimated torque $M_{em}^e$ (bottom trace) during the speed reversal transient. The stator resistance $R_s^*$ used within the controller is set to 120% of the actual $R_s$ value.

than the commanded value, but the torque–flux coupling is significantly more pronounced than in the case of correct $R_s$ tuning (Fig. 8). The drive response is, however, significantly degraded in the case of overestimated $R_s$ tuning (Fig. 10)—there exists a torque error in the steady state, the torque increase is uneven, and torque transients disturb the flux loop. Both the torque and flux loops are subject to oscillations whose amplitude and frequency increase with rise in motor speed and supply frequency $\omega_{dq}$; overestimates of $R_s$ larger than 20% even lead to instability and limit cycles above half of the rated speed. Problems related to overestimating $R_s$ are not uncommon in induction motor sensorless drives where the $dq$-frame speed is determined from stator voltage balance equations (10) and (11). This suggests two ways to address the problem in practice—either set the estimate of $R_s$ to a value slightly below the expected value, or adopt one of several online adaptation methods [13], [14], [21].

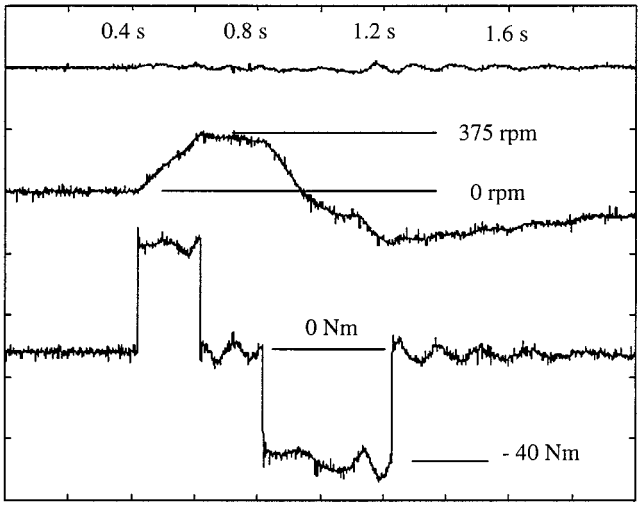


Fig. 11. Experimental traces of the estimated flux $\Psi_s^e$ (top trace), measured shaft speed $\omega_R$ (middle trace), and the estimated torque $M_{em}^e$ (bottom trace) during the speed reversal transient. The stator resistance $R_s^*$ used within the controller is set to 80% of the actual $R_s$ value.

## VIII. Conclusion

This paper has described a control architecture intended for low-cost medium-performance induction motor variable-speed drives, such as traction applications. The controller employs a single dc-link current sensor and no shaft sensors. The control algorithm is based on calculations of instantaneous active and reactive power from the dc-link current and PWM pattern. The algorithm is implemented in software and requires minimal additional hardware. The motor is controlled in a synchronous frame of reference whose speed is calculated from the instantaneous $P$ and $Q$ directly. The proposed controller was tested on a 7.5-kW induction motor drive. Sensitivities to errors due to lockout time and stator resistance detuning were investigated in a series of tests. The experiments confirm analytical results and verify the design guidelines presented in the paper.

## Appendix
## Experimental Setup Data

A 7.5-kW four-pole squirrel-cage induction motor is fed from an IGBT three-phase inverter. Two types of mechanical loading were made available. The motor is coupled either to a low-inertia frictional load, or to a separately excited dc motor. The dc-link voltage is obtained from a rectifier–battery setup, and kept at a constant level of $Udc = 138$ V. The dc-link current is measured by means of a Hall-effect current sensor. The detection circuitry given in Fig. 2 is built for this experiment. The control algorithm is implemented on a dual-processor digital drive controller with Dallas 80C320 and TI TMS320E14 microcontrollers. The motor/inverter parameters are as follows:

rated line-to-line voltage: $U_{\rm nom} = 90$ V;
rated current: $I_{\rm nom} = 58$ A;
rated frequency: $f_{\rm nom} = 52$ Hz;
equivalent leakage inductance: $L_e = 0.16$ (p.u.);
stator resistance: $R_s = 0.039$ (p.u.);
magnetizing inductance: $L_m = 1.92$ (p.u.);
rotor inductance: $L_r = 2$ (p.u.);

stator inductance: $L_s = 2$ (p.u.);
rotor resistance: $R_r = 0.043$ (p.u.);
rated torque at $\omega_{\rm nom}$: $T_{\rm nom1} = 45$ N·m;
rated torque at standstill: $T_{\rm nom2} = 35$ N·m;
when operating with the rated air-gap flux, the rated EMF at: $\omega_{\rm nom} = 1550$ r/min;
equivalent inertia of the ac motor and the dc brake: $J_1 = 0.2$ kg·m$^2$;
equivalent inertia of the ac motor connected to frictional load: $J_2 = 0.09$ kg·m$^2$;
IGBT inverter current limit at: $I_{\rm max} = 100$ A;
switching (PWM) frequency: $f_{\rm PWM} = 2$ kHz;
lockout time (deadtime): $\Delta t_{\rm lock} = 5$ $\mu$s.

## REFERENCES


[1] C. P. Henza and N. Mohan, "A digitally controlled AC to DC power conditioner that draws dinusoidal input current," in *Proc. IEEE PESC'86*, 1986, pp. 531–540.

[2] H. Akagi, Y. Kanagawa, and A. Nabae, "Instantaneous reactive power compensation comprising switching devices without energy storage components," *IEEE Trans. Ind. Applicat.*, vol. IA-20, pp. 625–630, May/June 1984.

[3] T. C. Green and B. W. Williams, "Derivation of motor line-current waveforms from the DC-link current of an inverter," *Proc. Inst. Elect. Eng.*, pt. B, vol. 136, no. 4, pp. 196–204, July 1989.

[4] ——, "Control of induction motors using phase current feedback derived from the DC link," in *Proc. EPE'89*, vol. 3, 1989, pp. 1391–1396.

[5] J. K. Pedersen and P. Thogersen, "Stator flux oriented asynchronous vector modulation for AC drives," in *Proc. IEEE PESC'90*, 1990, pp. 641–648.

[6] T. G. Habetler and D. M. Divan, "Control strategies for direct torque control using discrete pulse modulation," in *Conf. Rec. IEEE-IAS Annu. Meeting*, 1989, pp. 514–522.

[7] Y. Xue, X. Xu, T. G. Habetler, and D. M. Divan, "A low cost stator flux oriented voltage source variable speed drive," in *Conf. Rec. IEEE-IAS Annu. Meeting*, 1990, pp. 410–415.

[8] J. F. Moynihan, R. C. Kavanagh, M. G. Egan, and J. M. D. Murphy, "Indirect phase current detection for field oriented control of a permanent magnet synchronous motor drive," in *Proc. EPE'91*, vol. 3, 1991, pp. 641–646.

[9] B. K. Bose and M. G. Simoes, "Speed sensorless hybrid vector controlled induction motor drive," in *Conf. Rec. IEEE-IAS Annu. Meeting*, 1995, pp. 137–143.

[10] M. Riese, "Phase current reconstruction of a three phase voltage source inverter fed drive using sensor in the DC link," in *Proc. PCIM'96*, 1996, pp. 95–101.

[11] F. Blaabjerg and J. K. Pedersen, "A new low cost fully fault protected PWM-VSI inverter with true phase current information," in *Proc. IPEC'95*, vol. 2, 1995, pp. 984–991.

[12] T. Okuyama, N. Fujimoto, T. Matsui, and Y. Kubota, "A high performance speed control scheme for induction motor without speed and voltage sensors," in *Conf. Rec. IEEE-IAS Annu. Meeting*, 1986, pp. 106–111.

[13] T. G. Habetler, F. Profumo, G. Griva, M. Pastorelli, and A. Bettini, "Stator resistance tuning in a stator-flux field-oriented drive using an instantaneous hybrid flux estimator," *IEEE Trans. Power Electron.*, vol. 13, pp. 125–133, Jan. 1998.

[14] R. J. Kerkman, B. J. Seibel, T. M. Rowan, and D. Schlegel, "A new flux and stator resistance identifier for AC drive systems," in *Conf. Rec. IEEE-IAS Annu. Meeting*, 1995, pp. 310–318.

[15] F. Z. Peng and T. Fukao, "Robust speed identification for speed-sensorless vector control of induction motors," *IEEE Trans. Ind. Applicat.*, vol. 30, pp. 1234–1240, Sept./Oct. 1994.

[16] W. Leonhard, *Control of Electrical Drives*, 2nd ed. Berlin, Germany: Springer-Verlag, 1996.

[17] D. W. Novotny and T. A. Lipo, *Vector Control and Dynamics of AC Machines*. London, U.K.: Clarendon, 1996.

[18] J. Holtz, "State of the art controlled AC drives without speed sensor," in *Proc. PEDS'95*, vol. 1, 1995, pp. 1–6.

[19] ——, "Pulse width modulation for electronic power converters," in *Power Electronics and Variable Speed Drives*, B. K. Bose, Ed. Piscataway, NJ: IEEE Press, 1997, pp. 138–208.

[20] E. Holl, "Verfahren und Vorrichtung zur Buildung von Maschinenstromen einer Stromrichtergespeisten Drehfeldmaschine," European Patent 0502226A1, 1991.

[21] B. K. Bose and N. R. Patel, "A sensorless stator flux oriented vector controlled induction motor drive with neuro-fuzzy based performance enhancement," in *Conf. Rec. IEEE-IAS Annu. Meeting*, 1997, pp. 393–400.



**Slobodan N. Vukosavic** (M'94) was born in Sarajevo, Bosnia and Hercegovina,Yugoslavia, in 1962. He received the B.S., M.S., and Ph.D. degrees from the Electrical Engineering Faculty, University of Belgrade, Belgrade, Yugoslavia, in 1985, 1987, and 1989, respectively.

Since 1986, he has been with the Nikola Tesla Institute, Belgrade, Yugoslavia, where he conducts research in the areas of static power converters and microcomputer-based control of electrical drives. He is currently with the Department of Electrical Engineering, University of Belgrade, where he teaches undergraduate and graduate courses in power electronics and control of electrical drives. In 1988, he spent six months with the ESCD Laboratory, Emerson Electric Company, St. Louis, MO, in a cooperative research program. Since October 1991, he has been associated with Vickers Electric Company, Milan, Italy, as a part of a research program in the design and control of electrical drives for robots. His scientific interests are in the areas of system modeling and identification, microcomputer-based real-time control, power electronics, and rotating electrical machines design and control.

**Aleksandar M. Stankovic** (S'88–M'91) received the Dipl. Ing. and M.S. degrees from the University of Belgrade, Belgrade, Yugoslavia, and the Ph.D. degree from Massachusetts Institute of Technology, Cambridge, in 1982, 1986, and 1993, respectively, all in electrical engineering.

Since 1993, he has been with the Department of Electrical and Computer Engineering, Northeastern University, Boston, MA, where he is currently an Associate Professor. He spent the 1999/2000 school year on sabbatical at the United Technologies Research Center and the Otis Elevator Engineering Center.

Dr. Stankovic is a member of the IEEE Power Engineering, IEEE Power Electronics, IEEE Control Systems, IEEE Circuits and Systems, IEEE Industrial Electronics and IEEE Industry Applications Societies. He serves as an Associate Editor of the IEEE TRANSACTIONS ON CONTROL SYSTEMS TECHNOLOGY and as Chair of the Technical Committee on Power Electronics and Power Systems of the IEEE Circuits and Systems Society.